Layer dependence of defect charge transition levels in two-dimensional materials

Dan Wang* and Ravishankar Sundararaman†
Department of Materials Science and Engineering, Rensselaer Polytechnic Institute, 110 8th Street, Troy, New York 12180, USA

(Received 4 November 2019; revised manuscript received 28 January 2020; accepted 29 January 2020; published 10 February 2020)

Point defects in two-dimensional (2D) materials hold great promise for optoelectronic and quantum technologies. Their properties depend sensitively on the dielectric environment and number of 2D layers, but this has remained a challenge to include in first-principles calculations on account of the high computational cost. Recent first-principles techniques facilitate efficient prediction of substrate effects on defect charge transition levels in 2D materials, replacing the substrate by a continuum dielectric model. Here, we show that analogous continuum treatment of defect-free layers in multilayer 2D materials accurately predicts defect energies compared to explicit multilayer calculations, but at a small fraction of the computational cost. Applications of this technique to one- to five-layer and bulk hexagonal boron nitride reveal that defect ionization energies systematically decrease with an increasing number of layers and for defects in inner layers due to increased dielectric screening. Our results highlight the dominant role of electrostatic screening in the effect of the environment and the feasibility of tuning defect levels in 2D materials using material thickness and defect location within the material.

DOI: 10.1103/PhysRevB.101.054103

I. INTRODUCTION

Defects in two-dimensional (2D) materials are of great importance in a wide range of technological applications, including electronic computing and quantum information [1–4]. Both naturally occurring defects, such as vacancies and oxygen substitutions, and intentional doping considerably affect material properties and device performance [5–12]. Defect engineering is an essential step in device fabrication, including controlled implantation of donors and acceptors to produce *pn* junctions in 2D semiconductors [13–15] and of high spin defects in wide-band-gap materials such as qubits and single-photon emitters for quantum technologies [16–19]. A comprehensive understanding of defects in 2D materials is therefore critical for the advancement of these applications.

First-principles calculations based on density-functional theory (DFT) play a central role in computational materials design, including for defects in three-dimensional (3D) and 2D materials. Recent computational developments to correct for previously challenging finite-size supercell errors in charged defects have led to a rapid exploration of the stability and charge transition levels of defects in 2D materials [20–27]. Yet most defect calculations focus on monolayer materials, and defect predictions for multilayer systems are not widely reported despite the fact that most experimental realizations of devices such as single-photon emitters employ multilayer 2D materials. Notably, high environment sensitivity of defects in 2D materials [23,28–31] suggests a correspondingly strong dependence on the number of layers in multilayer 2D materials, making the treatment of such environment and adjacent layer effects indispensable.

However, evaluating defects in multilayer materials is rather challenging due to the high computational cost, with an N-layer system typically requiring N^3 more computational time than a monolayer in DFT calculations. This cost is further exacerbated by the requirement of beyond-DFT treatment, such as using GW many-body perturbation theory, to accurately predict energy level alignment and band edge positions [32]. In particular, a typical five-layer material will already require two orders of magnitude more computational effort than a monolayer for each defect, making computational screening of several defect candidates computationally prohibitive and necessitating the development of more efficient techniques. We recently developed a computationally efficient approach that accurately accounts for substrate effects on defects in first-principles calculations of the 2D material alone, treating the substrate using a continuum model of its dielectric response and thereby removing a large number of substrate atoms and electrons from the quantum-mechanical calculation [33]. One possibility of reducing the computational requirements for multilayer materials is to regard the defect-free layers as a "substrate" and then apply the continuum model. However, the similarity in energy levels between each layer in multilayer systems could lead to larger electronic interactions (beyond the mean-field electrostatic response), and it is not intuitively clear if a continuum approach could be accurate for multilayer materials.

In this paper, we demonstrate that a first-principles with continuum model approach can accurately predict defect properties in multilayer 2D materials at a fraction of the computational cost by excluding the defect-free layers from the DFT calculation. With hexagonal boron nitride (hBN) as a prototypical example, we investigate the variation of the defect transition levels as a function of layer number [from monolayer (1L) up to five-layer (5L) and bulk] and the level dependence on defect location. We specifically focus on

*wangd11@rpi.edu
†sundar@rpi.edu

 ©2020 American Physical Society

defects of interest for quantum information, including carbon substitutions (C_B and C_N) and substitution-vacancy complexes ($C_B V_N$ and $C_N V_B$), accounting for all inequivalent doping sites. With increasing layer number, charge transition levels of donors move towards the vacuum level, whereas those of acceptors move in the opposite direction, decreasing the ionization energies in both cases. We validate the accuracy of these predictions by comparison to much more expensive calculations of explicit multilayer materials in a few selected cases. The good agreement between the continuum model and explicit calculations not only shows the accuracy of the model for rapid exploration of defects in multilayer materials but also implies that the electrostatic screening captured by the continuum model dominates the environmental effects on defects in 2D materials. Finally, using many-body GW calculations to correct for self-interaction errors and account for the nonlocal screening effect, we show that accurate description of the band edge position is vital for accurate defect ionization energy predictions.

II. THEORY AND METHODS

A. Defect transition level and ionization energy

The formation energy of a defect with charge q is [34–36]

$$E_f(D, q) = E_{\text{tot}}(D, q) - E_{\text{host}} + \sum_i n_i\mu_i + q\mu_e + E_{\text{corr}}, \tag{1}$$

where $E_{\text{tot}}(D, q)$ is the total energy of the system with the defect, E_{host} is the energy of the perfect host, n_i and μ_i are the number and chemical potential of atom i (e.g., C, B, N) being exchanged during the defect formation, μ_e is the Fermi energy ranging from valence band maximum (VBM) to the conduction band minimum (CBM), and E_{corr} is a correction term for the total energy of supercells with charged defects.

The atomic chemical potentials μ_i depend on the growth conditions and the source for potential substitutional impurities. Specifically, for hexagonal boron nitride in thermodynamic equilibrium, $\mu_B + \mu_N = \mu_{BN}^{1L}$ for 1L hBN, and $\mu_B + \mu_N = \mu_{BN}^{\text{bulk}}$ for bulk hBN, where μ_{BN}^{1L} and μ_{BN}^{bulk} are the total energy per formula unit of freestanding and bulk hBN, respectively. The specific values of μ_B and μ_N then depend on which species is more abundant: μ_B is set to the per-atom energy in α-rhombohedral boron in the B-rich condition, while μ_N is set to the per-atom energy in N_2 in the N-rich condition, with the other chemical potential determined from the sum (μ_{BN}) constraint in each case. For substitutional defects including carbon atoms, we refer μ_C to the per-atom energy in graphene.

Calculations with $q \neq 0$ require a correction scheme to remove the spurious Coulomb interaction of the net charge with its periodic images and the compensating background charges. Here, we employ a model-charge correction scheme [21,22] which determines E_{corr} from the electrostatics of a Gaussian charge in a dielectric slab model mimicking the 2D defect. Solving the Poisson equation for this model using both isolated boundary conditions and the same periodic boundary conditions as the DFT calculations provides a prediction of the spurious interactions to subtract. (See the Supplemental Material [37], Refs. [21,22] for details.)

Finally, the defect charge transition level $\epsilon(q/q')$ is defined as the Fermi energy μ_e in Eq. (1), for which $E_f(D, q) = E_f(D, q')$, resulting in

$$\epsilon(q/q') = \frac{E_{\text{tot}}(D, q) + E_{\text{corr}}(q) - E_{\text{tot}}(D, q') - E_{\text{corr}}(q')}{q' - q}. \tag{2}$$

The defect ionization energy is then the difference between $\epsilon(q/q')$ and the corresponding band edge (VBM for acceptors and CBM for donors), which corresponds to the energy required to free electrons or holes.

B. Continuum model for 2D multilayer systems

The computational challenge of including the effect of hundreds of environment atoms in first-principles calculations of charged defects can be addressed by replacing these atoms by the dielectric screening of a continuum model [33]. Briefly, this method captures the dominant electrostatic interaction of the environment by placing the defective 2D layer of interest next to a dielectric function profile $\varepsilon(z)$ of the environment calculated from first principles. The only unknown parameter is then the spatial separation between the explicit DFT layer and the continuum environment, which is set by equating $E_{\text{int}}^{\text{DFT}} = E_{\text{int}}^{\varepsilon(z)}$, where $E_{\text{int}}^{\text{DFT}}$ and $E_{\text{int}}^{\varepsilon(z)}$ are the interaction energies of a Gaussian test charge with the real substrate and with the $\varepsilon(z)$ model, respectively. Analogous to continuum solvation models for liquid environments developed for the treatment of solid-liquid interfaces [38–43], the dielectric model $\varepsilon(z)$ is described using a shape function $s(z)$ which smoothly transitions from 0 (vacuum region) to 1 (dielectric slab region) as $\varepsilon(z) = 1 + (\varepsilon_b - 1)s(z)$, where ε_b is the dielectric constant of the substrate. The self-consistent solution of the modified Poisson equation with the dielectric profile $\varepsilon(z)$ augments the Hartree potential term in the DFT Hamiltonian, and the resulting DFT total energies then automatically include the dominant electrostatic interaction of the substrate with the charge distribution of the 2D material and defect. (See Ref. [33] for additional details.)

We find here that this continuum model approach works remarkably well not only for defects in 2D materials on substrates [33] but also for defects in multilayer 2D materials. In this case, we replace the dielectric effect of the defect-free layers by a dielectric function profile $\varepsilon(z)$. Unlike the treatment of 3D substrate materials which can be approximated by a spatially uniform dielectric response in their interior, the treatment of 2D layers requires treatment of the spatially inhomogeneous response. Therefore, we directly obtain $\varepsilon(z)$ from DFT calculations of the surrounding layers, analogous to the procedure for constructing the dielectric profile for the charged defect correction [21], instead of from a shape function $s(z)$ modulating the bulk dielectric constant. Specifically, we apply a small normal electric field E_0 to the defect-free layers of the slab, calculate the change in the total electrostatic potential $\Delta V(z)$, and find $\varepsilon^{-1}(z) = -\frac{1}{E_0}\frac{\partial \Delta V(z)}{\partial z}$. The atomic geometry is self-consistently optimized in all calculations presented here, including in this dielectric calculation, which makes it the low-frequency dielectric function $\varepsilon_0(z)$ [instead of the high-frequency value $\varepsilon_\infty(z)$ if atomic geometries were constrained throughout]. See Ref. [21] for details.

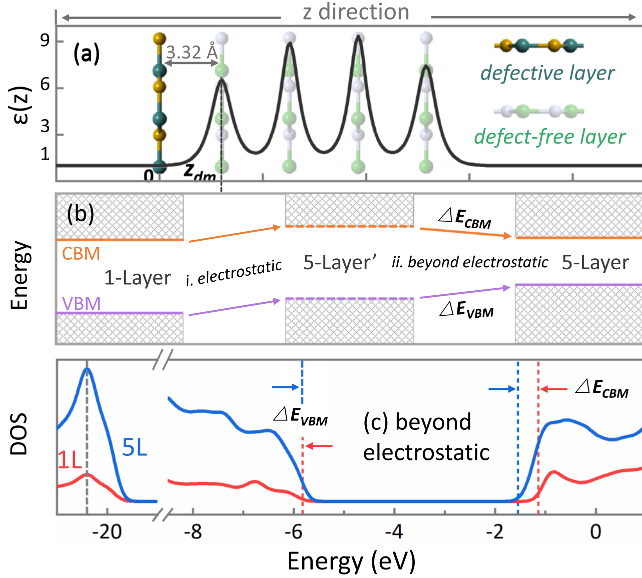

FIG. 1. (a) Continuum model treatment of defects in an outer layer of five-layer hBN, specified by the dielectric function $\varepsilon(z)$. The layer containing the defect is placed at $z = 0$, and the nearest peak of $\varepsilon(z)$ is z_{dm} away. (b) Scheme for determining band edge positions of the five-layer system in the continuum approach, accounting for the rigid shift due to the electrostatic potential from the continuum model calculation and edge shifts (ΔE_{CBM}, ΔE_{VBM}) from (c) an explicit density-of-states calculation of the five-layer system. After aligning the core levels (gray dashed line) with that in 1L, the difference in the band edges (dashed red and blue lines) yields ΔE_{CBM} and ΔE_{VBM}.

Figure 1(a) illustrates the example of 5L hBN with a defect on the surface layer. Without loss of generality, the defective atomic layer is at $z = 0$, and the nearest peak of the dielectric function of the defect-free layer is located at $z = z_{dm}$. The $\varepsilon(z)$ obtained directly from DFT calculations enables z_{dm} to be set to the explicit interlayer spacing distance, making the overall procedure for multilayer systems easier than 2D materials on substrates (which required a separate determination of z_{dm}) [33]. The net $\varepsilon(z)$ profiles for 2L, 3L, 4L, and 5L hBN with all possible inequivalent defect locations (surface, second layer, innermost layer, etc.) are shown in Fig. S1 of the Supplemental Material [37].

The dielectric function profile in the continuum model essentially introduces a net dipole in that layer, which creates a shift of the net DFT electrostatic potential from one side of the continuum model layer to the other, effectively shifting the potential in the layer treated explicitly relative to the vacuum level. Also, the change in the electrostatic potential does not have a significant spatial variation in the region of the explicit layer (since the model does not overlap with that region). Therefore, the continuum model shifts the VBM and CBM equally. This leaves the band gap unchanged, as shown in Fig. 1(b) (left panel, from 1-layer to 5-layer′). Effects beyond the electrostatic interaction are captured by aligning explicit density of states calculations of the defect-free multilayers with the monolayer, as shown in Fig. 1(c), closely mimicking the corresponding procedure for substrate effects [33]. After aligning the core levels for 1L and 5L hBN to remove the electrostatic potential contributions, the differences in band edge positions yield the offsets ΔE_{VBM} and ΔE_{CBM}. The final band edge positions combine the electrostatic and beyond-electrostatic effects together, as shown in Fig. 1(b) (right panel, from 5-layer′ to 5-layer). For example, in 5L hBN, the continuum model shifts both the VBM and CBM up by 0.940 eV, while the band edge offsets are $\Delta E_{\text{VBM}} = -0.002$ eV and $\Delta E_{\text{CBM}} = -0.406$ eV after aligning the core energy levels. Therefore, the net VBM and CBM energy corrections for referencing the continuum model results are $E^{5L}_{\text{VBM}} - E^{1L}_{\text{VBM}} = 0.940 - 0.002 = 0.938$ eV and $E^{5L}_{\text{CBM}} - E^{1L}_{\text{CBM}} = 0.940 - 0.406 = 0.534$ eV. Below, we use exactly the same procedure to refine the band edge positions using GW many-body perturbation theory, using an additional offset for each band edge from DFT to GW calculations of the defect-free multilayer.

C. Computational details

Calculations necessary to obtain the results discussed here include supercells of monolayer (1L), few-layer (2L to 5L), and bulk hBN with and without defects. We implement the above methods in and perform DFT calculations using the open-source plane-wave DFT software JDFTX [44], with the Garrity-Bennett-Rabe-Vanderbilt ultrasoft pseudopotentials [45], Perdew-Burke-Ernzerhof (PBE) generalized gradient approximation [46] to the exchange-correlation functional, and plane-wave kinetic energy cutoffs of 20 hartrees for wave functions and 100 hartrees for the charge density. Brillouin zone sampling employs a Monkhorst-Pack k mesh of $2 \times 2 \times 1$ for $6 \times 6 \times 1$ supercells of the 1L to 5L hBN primitive cell. The cell size in the z direction (normal to the 2D material plane) is 16 Å for 1L hBN and 30 Å for 2L–5L hBN, with Coulomb truncation to eliminate interactions with periodic images along z [47].

Defects in bulk hBN are computed with a $6 \times 6 \times 2$ supercell of the energetically favorable AA′ stacking eclipsed with N over B [48], resulting in four total layers per simulation cell, with a $2 \times 2 \times 2$ k mesh for Brillouin zone integration. Van der Waals correction with the dispersion-corrected DFT (DFT-D2) scheme [49] is used throughout to get an appropriate layer spacing. Specifically, for the bulk, we obtain a lattice constant of $a = 2.51$ Å and an interlayer spacing of $c = 3.32$ Å, in agreement with previous reports [48]. All atoms are allowed to relax in all calculations, including in the dielectric function calculation for the continuum model, as discussed above.

D. GW calculations and convergence

We perform GW quasiparticle band-structure calculations of 1L–3L and bulk hBN unit cells using BERKELEYGW [50]. Specifically, we perform one-shot G_0W_0 calculations from a PBE-DFT starting point generated by JDFTX [44] with the optimized norm-conserving Vanderbilt norm-conserving pseudopotentials [51] and a plane-wave kinetic energy cutoff of 70 Ry. Accurate band edge positions and band gaps in GW calculations, especially for 2D materials, require careful convergence of the GW results [52–54]. Here, the cell sizes normal to the atomic plane for 1L, 2L, and 3L hBN are 16, 19, and 23 Å, respectively, with Coulomb truncation used to speed up the convergence. Increasing further to 18.5 Å for

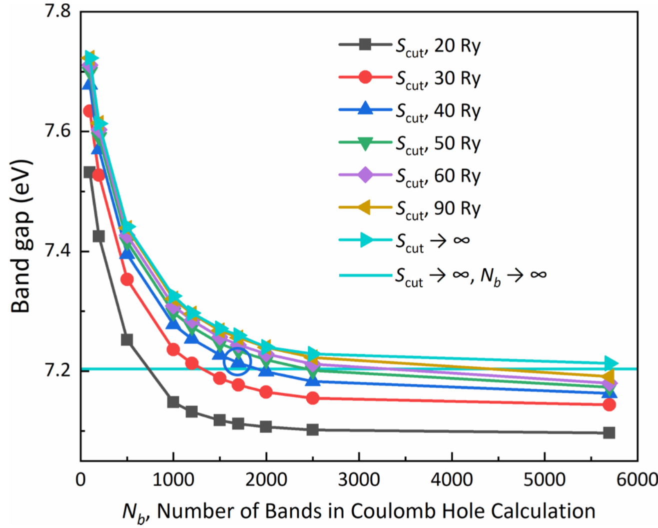

FIG. 2. Convergence of GW calculations of the quasiparticle band gap of monolayer hBN with the number of bands included in the Coulomb hole summations N_b and the energy cutoff for the dielectric matrix S_{cut} with an "infinite" number of empty bands for the dielectric matrix N_c (approaching the number of plane waves) and a $12 \times 12 \times 1$ k mesh. Values at $S_{\mathrm{cut}} \to \infty$ are extrapolated using the 40–90 Ry results to infinite energy cutoff. The azure solid line represents the "final" extrapolated result at $S_{\mathrm{cut}} \to \infty$ and $N_b \to \infty$. The blue circle represents the band gap at the chosen parameters of $S_{\mathrm{cut}} = 40$ Ry and $N_b = 1700$.

1L hBN changes the band gap by only 60 meV. The final GW values used below are extrapolated to the infinite k-point limit using $9 \times 9 \times 1$ and $12 \times 12 \times 1$ k-mesh results for each of the 1L–3L systems based on the technique proposed in Ref. [22], while the bulk hBN results are as obtained directly with a $12 \times 12 \times 4$ k mesh. Adding two more k-mesh settings (i.e., $10 \times 10 \times 1$ and $11 \times 11 \times 1$) to the extrapolation for 1L hBN almost does not change the final value, demonstrating the GW results are well converged with respect to the k-space samplings.

In addition, plane-wave GW calculations require convergence with respect to the number of empty states N_c, the kinetic-energy cutoff for the dielectric matrix/screened Coulomb interaction S_{cut}, and the number of bands included in the Coulomb hole summations N_b [50,54]. Figure 2 summarizes the GW convergence tests for 1L hBN. We use an "infinite" $N_c = 5700$ close to the total number of plane waves in the wave function basis and test gap errors with respect to N_b and S_{cut}. For each N_b, we can extrapolate the results to $S_{\mathrm{cut}} \to \infty$, and for each S_{cut}, we can extrapolate the results to $N_b \to \infty$. (See Fig. S2 in the Supplemental Material [37] for additional details on the extrapolation and overall GW convergence tests.) Using the $N_b \to \infty$ and $S_{\mathrm{cut}} \to \infty$ result of $E_g = 7.203$ eV (azure line in Fig. 2) as a reference, we determine appropriate N_b and S_{cut} that provide answers converged to a target accuracy of 0.1 eV. Specifically, the $N_b \to \infty$ limit of $S_{\mathrm{cut}} = 40$ Ry and the $S_{\mathrm{cut}} \to \infty$ limit of $N_b = 1700$ are each within 0.1 eV of this final result. Note that the convergence errors with respect to N_b and S_{cut} tend to cancel, such that the result with these parameters (blue circle in Fig. 2) is effectively accurate to much better than 0.1 eV. Using these convergence tests, we select $S_{\mathrm{cut}} = 40$ Ry for multilayer and bulk calculations, scale N_b proportional to the unit cell volume relative to 1700 for the monolayer since it is plane wave dependent, and set N_c to the basis-limited infinite value in all cases. We further set N_b to the basis-limited infinite value for the computationally simpler bulk case to guarantee convergence.

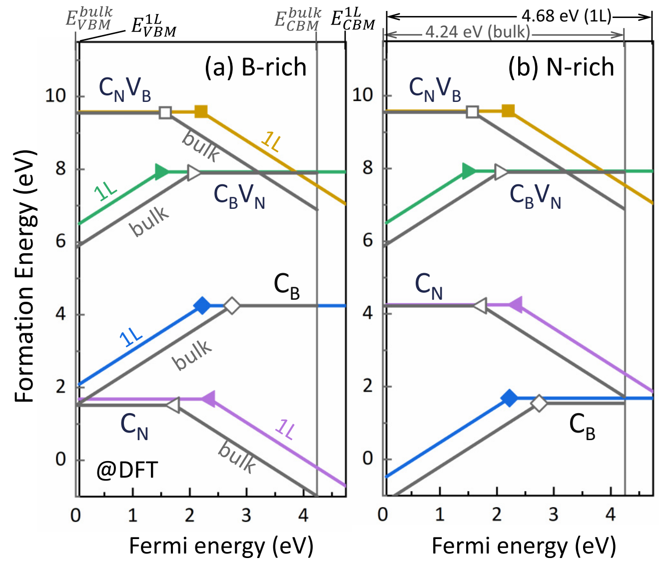

FIG. 3. Predicted formation energies of C_B, C_N, C_BV_N and C_NV_B in neutral and singly charged states (+1 for donors and −1 for acceptors) as a function of Fermi energy under (a) B-rich and (b) N-rich conditions. Colored lines and solid symbols denote formation energies and charge transition levels of these defects in monolayer (1L) hBN, while gray lines and open symbols denote them for the bulk hBN case. Black and gray vertical lines mark the corresponding band edge positions. Neutral defects shift by less than 0.1 eV, while charged defects are stabilized by ≈0.60 eV from 1L to bulk, resulting in an ≈0.56 eV reduction in acceptor ionization energies and ≈1.05 eV reduction in donor ionization energies after accounting for small VBM and larger CBM shifts.

III. RESULTS AND DISCUSSION

A dielectric environment surrounding a 2D material augments its screening and weakens the long-range Coulomb interaction between charges. The charge transition level $\epsilon(q/0)$ is the energy difference between the formation energies of a defect in charged and neutral states [Eq. (2)], and the change in screening primarily impacts the charged formation energy. This should result in shallower transition levels or lower ionization energies for defects with increased screening by each additional layer of the 2D material, with the 3D bulk material being the asymptotic limit with respect to the number of layers. Below, we quantitatively show that this is precisely the behavior for defects in multilayer hBN, using both our continuum model approach detailed above and explicit multilayer DFT calculations as a benchmark.

To set the stage for this layer-dependent variation, Fig. 3 first compares the DFT-predicted formation energies of the two endpoints: 1L and bulk hBN. It shows results for C_B, C_N,

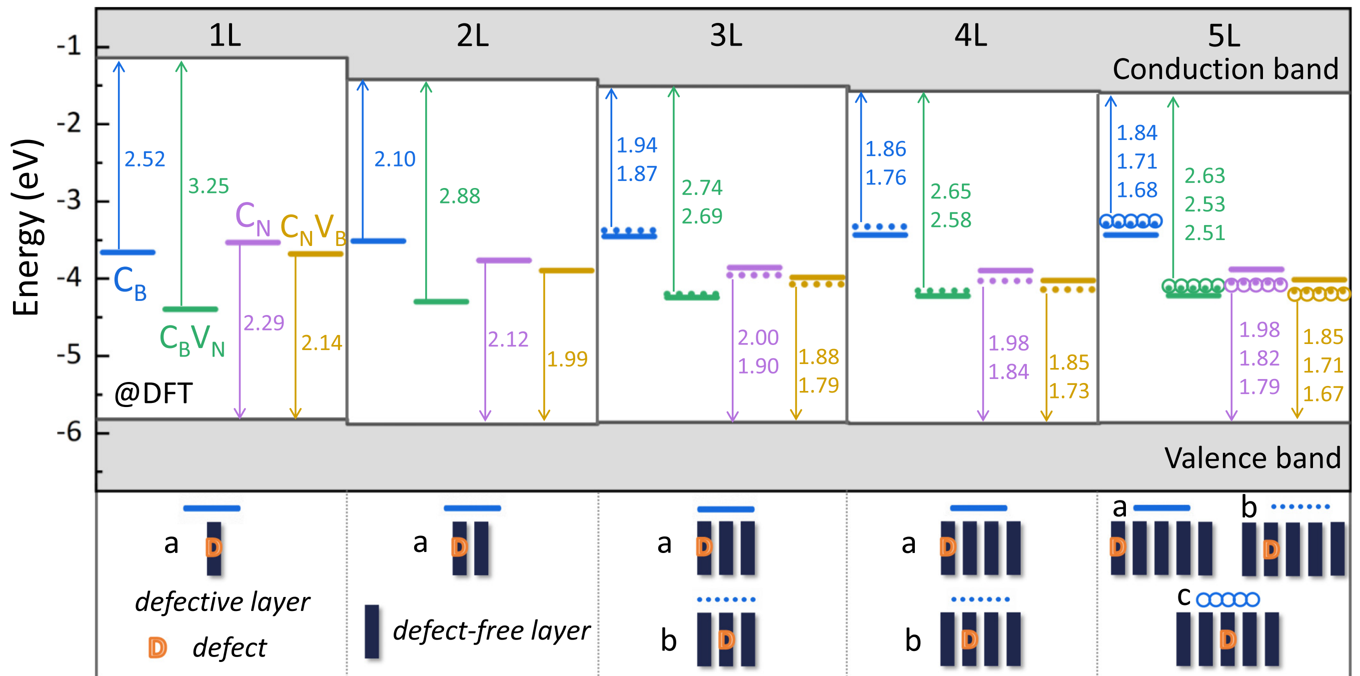

FIG. 4. Charge transitions levels of C_B, C_N, C_BV_N, and C_NV_B in 1L to 5L hBN for all possible nonequivalent placements (e.g., surface, inner, or central layer) of the defect shown in the lower panel. Ionization energies labeling the arrows are sorted from outermost to innermost layer placement of the defect. With respect to the vacuum level as the zero of the energy axis, the conduction band moves downwards with increasing levels much more substantially than the valence band, amplifying the ionization energy reduction of donors compared to acceptors.

C_BV_N, and C_NV_B as a function of the Fermi level position (electron chemical potential) in both B- and N-rich conditions. Note that the Fermi level is referenced to the VBM, which moves downward by 0.06 eV from 1L to bulk (at equal electrostatic potentials based on core-level alignment), while the CBM moves downward by 0.50 eV, resulting in a band gap reduction of 0.44 eV at the DFT level (from 4.68 eV in 1L to 4.24 eV in bulk hBN). The band edge shifts and the corresponding band gap increases from bulk to 1L hBN are due to the quantum confinement effect. The more substantial CBM shift than VBM shift can be understood by the more delocalized state around CBM than VBM (a smaller effective mass of the conduction band compared to that of the valence band) [55]. C_B and C_BV_N are donorlike defects with charge state transition from +1 to 0, whereas C_N and C_NV_B are acceptorlike defects with charge state transition from 0 to −1. The formation of neutral C_B and C_N is energetically favorable under N-rich and B-rich conditions, respectively, while the relative stability of neutral C_BV_N and C_NV_B is independent of N and B abundance (since it involves removal of an entire BN unit).

The neutral formation energies of all defects shown in Fig. 3 change very slightly when the defects are transferred from 1L to bulk hBN, with the most noticeable differences for C_N in B-rich conditions and C_B in N-rich conditions (still less than 0.1 eV). On the other hand, all charged defects are significantly stabilized (lower ionization energies) in the bulk due to the additional screening, as expected. Specifically, the donor ionization energies (downward relative to CBM) decrease from 2.52 to 1.49 eV for C_B and 3.25 to 2.18 eV for C_BV_N, while the acceptor ionization energies (upward relative to VBM) decrease from 2.28 to 1.73 eV for C_N and 2.14 to 1.57 eV for C_NV_B, irrespective of atomic chemical potentials (N/B rich), which cancel out in the energy difference. Notice that the donor levels both shift by about 1.05 eV, while the acceptor levels both shift by about 0.56 eV. The larger reduction for donors comes from the significant downward shift of the CBM. The small downward shift of the VBM would tend to increase acceptor ionization energies, but it is negligible compared to the screening effect that works to reduce them.

Calculating defect energetics in multilayer 2D materials is significantly more expensive than in the monolayer and bulk limits discussed above. We use the continuum model approach to systematically map the impact of the number of layers (ranging from two to five) and defect position within the multilayer stack on the transition levels of each of these defects, as shown in Fig. 4. We benchmark the accuracy of the continuum model against much more expensive, explicit all-atom calculations for selected defects (C_B in 2L, 3L, and 5L and C_N in 2L) and find ionization energy predictions to be accurate within 0.05 eV in all cases. (See Table S2 in the Supplemental Material [37] for these ionization energy comparisons.) The excellent accuracy of the continuum model also implies that the electrostatic screening captured by the model is the dominant factor of the environmental effects on defects in 2D materials.

Figure 4 illustrates that the DFT band gap of hBN decreases monotonically from 4.68 to 4.28 eV with increasing layers, with the CBM shifting more substantially than the VBM. As in the comparison of defects between monolayer and bulk hBN above, this makes the ionization energies of donors more sensitive with respect to layer number than those of acceptors. Specifically, the maximum reduction in

ionization energies (from 1L to 5L-c) is 0.84 and 0.74 eV for C_B and C_BV_N donors, compared to 0.50 and 0.47 eV for C_N and C_NV_B acceptors. Also note that the shifts for the 5L case (relative to 1L) are still about 0.1–0.3 eV smaller than those for the bulk, indicating that the screening effect due to individual layers is rather weak and two to four layers still do not screen the Coulomb potential of the defects completely.

The multilayer material with $N > 2$ additionally contains multiple nonequivalent choices of the defect position, which also has an effect on the transition level. Taking C_B in 5L hBN as an example (Fig. 4), the transition level moves up by 0.13 eV (from −3.43 to −3.30 eV) when the defect is moved from the outermost layer (5L-a in Fig. 4) to the second layer (5L-b) and further goes to −3.27 eV when it is moved to the third (innermost) layer (5L-c). The other defects have a similar tendency: the donor (acceptor) transition level shifts up (down) by 0.1–0.16 eV from 5L-a to 5L-b and further shifts by only 0.02–0.04 eV to 5L-c. As expected, defects in inner and central layers experience increased screening from both sides and are therefore shallower than defects in surface layers. The neutral defect has very similar energy regardless of the location (validated by explicit DFT calculations of neutral C_B in 5L-a, 5L-b, and 5L-c), indicating that the neutral defect may form with equal probability in each layer of 5L hBN. However, the defects in the inner and central layers are more likely to achieve the excitation of $\text{Donor}^0 \rightarrow \text{Donor}^{+1} + e^{-1}$ or $\text{Acceptor}^0 \rightarrow \text{Acceptor}^{-1} + h^{+1}$, where e^{-1} is a conduction electron and h^{+1} is a valence hole due to the smaller ionization energy. Therefore, dopants for 2D semiconductors (requiring shallower defects) and defect states designed for long coherence times (requiring deeper defects) would be preferable in the inner and central layers and surface layers, respectively. Also, the slight difference (comparable to k_BT at room temperature) between 5L-b and 5L-c (because the screening strength is inversely proportional to the distance) indicates that the defects in all layers other than the surface layer in a system with $N \geqslant 5$ can be considered to have similar electronic properties. This is a very important point as precise experimental control of defect location is usually challenging.

Given that most devices with multilayer 2D materials would also involve a substrate, we also calculate the ionization energy of C_B in 5L hBN on H-passivated diamond(111) using the continuum model approach. Here, only one explicit hBN layer containing the defect is included in the quantum-mechanical calculations, treating all remaining layers and the substrate as a continuum. (See Ref. [33] for details regarding the dielectric profile of the diamond substrate.) Due to the asymmetry of the system, C_B now has five inequivalent sites. The corresponding ionization energies are 1.583, 1.423, 1.382, 1.377, and 1.384 eV, respectively, for a defect placed from the top layer (farthest from the diamond) to the bottom layer (nearest the diamond). The placement of the 5L hBN on the substrate of diamond decreases the defect ionization energy by about 0.3 eV. The slight increase of the ionization energy from 1.377 eV (the second-nearest layer to the diamond) to 1.384 eV (the nearest layer to the diamond) can be ascribed to stronger in-plane screening by adjacent hBN layers compared to the diamond substrate.

In addition, to check the effect of the location of the explicit/dielectric interface relative to the defect in the continuum model, we also calculated the ionization energy of C_B in 5L hBN with M explicit atomic layers and M' dielectric function layers ($M + M' = 5$), as shown in Table S3 of the Supplemental Material [37]. The explicit layer containing the defect is always put in the central position (i.e., 5L-c). The errors of a continuum model with $M = 1$, 3, and 4, compared to explicit DFT calculations ($M = 5$), are all well within 0.04 eV. We reiterate that all energies presented in Fig. 4 are obtained with only one explicit atomic layer.

So far, we have presented predictions of charge transition levels and ionization energies at the semilocal DFT (PBE) level. As is well known, semilocal DFT underestimates band gaps and is inaccurate for band edge positions, thereby significantly influencing the defect ionization energy [28,56,57]. GW many-body perturbation theory can rectify these issues but is extremely expensive for large supercell calculations containing defects. Fortunately, referenced to the vacuum level, defect transition levels in 2D hBN are found to be extremely insensitive to the level of theory, remaining unchanged between PBE and GW to within 0.1 eV [58]. (This is primarily because charge transition levels are obtained from the differences in total energies, which tend to be accurate in DFT, unlike band edge positions, which are electronic eigenvalues known to be unreliable.) Therefore, the primary impact of GW corrections is on the band edge positions, which we focus on below. We can therefore simply reference the previous defect transition levels computed using PBE-DFT on a large defect supercell to accurate band edge positions computed using GW on primitive cells of the undefective material (with varying layer number). This allows combining the computational efficiency of PBE-DFT for large supercells with the accuracy of GW for the band positions to rapidly obtain accurate ionization energy predictions.

Figure 5(a) shows the GW-predicted band edge positions with respect to the vacuum level for 1L to 3L and bulk hBN, which are in excellent agreement with previous GW predictions using a different (without empty states) technique [58]. (See Table S1 in the Supplemental Material [37] for a detailed comparison.) Going from 1L to bulk, the shifts in CBM and VBM are, respectively, −0.62 and +0.44 eV in GW, compared to −0.50 and −0.06 eV in DFT, as discussed above, revealing the correction of a much stronger self-interaction error in the VBM position.

Note that the GW gap reduction from 1L to 3L is 0.21 eV, which is only 20% of the 1.05-eV reduction from 1L to the bulk. In comparison, the DFT band gap decreased by 0.33 eV from 1L to 3L, which is 75% of the net reduction of 0.44 eV from 1L to the bulk. Therefore, the overall gap reduction is larger in GW than in DFT, as is well known and expected due to the impact of dielectric screening on energy levels in GW (captured via the screened Coulomb interaction W) that is missed by DFT. However, for the few-layer cases, the band gap reduction is unexpectedly *larger* in DFT, primarily because only a small fraction of the screening effects that eventually lead to the large bulk GW band gap reduction is captured in the first few surrounding layers.

Finally, referencing the defect transition levels from Fig. 4 (specifically for 1L, 2L, and 3L-b) with respect to the GW

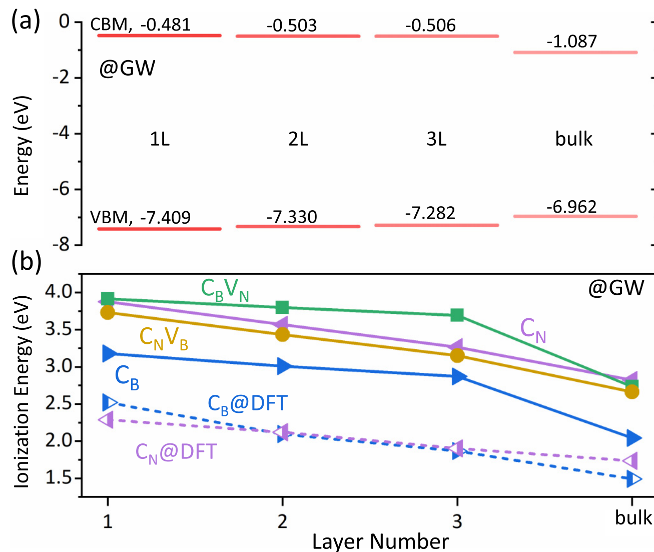

FIG. 5. (a) Band positions relative to the vacuum level from GW calculations. (b) Defect ionization energies relative to GW band edges as a function of the layer number. DFT ionization energies of C_B and C_N shown for comparison using dashed lines and half-filled triangles. GW increases all ionization energies, weakens the variation of the donor ionization energy with layers due to reduced variation of the CBM position, and strengthens the variation of acceptor ionization energy to greater variation of the VBM position.

band edge positions, Fig. 5(b) shows the final ionization energy predictions for the four defects. Compared to the previous DFT results, the band position changes discussed above lead to an overall increase in all the defect ionization energies. Additionally, the ionization energy variation of donors becomes weaker with the number of layers due to reduced shifting of the CBM, while that for acceptors becomes stronger due to increased shifting of the VBM.

IV. CONCLUSIONS

We have shown that defect ionization energies in 2D materials are sensitive to the number of layers and the position of the defect within the stack of layers. Intuitively, the ionization energies of defects systematically decrease due to increased dielectric screening and corresponding stabilization of the charged defect state with an increasing number of layers and as the defect is closer to the center of a multilayer stack. While DFT calculates accurate charge transition levels relative to vacuum, GW calculations of the band edge positions are vital to correctly describe the ionization energies. In fact, smaller variations of the CBM and stronger layer-dependent modifications of VBM positions in GW qualitatively change the trend of ionization energy reduction with layers for donor and acceptor defects.

We also showcased the efficacy and accuracy of a continuum model approach to describe the impact of adjacent layers in a multilayer material. Replacing adjacent layers by a continuum dielectric response substantially reduces the number of atoms and electrons in the electronic structure component and retains an accuracy of 0.05 eV with respect to explicit DFT multilayer calculations. The general framework we have developed here will prove useful for rapid evaluation of point defect properties in 2D materials and their heterostructures, laying the foundation for high-throughput computational screening for desirable material-defect pairs for microelectronic, optoelectronic, and quantum information applications.

ACKNOWLEDGMENTS

We acknowledge startup funding from the Department of Materials Science and Engineering at Rensselaer Polytechnic Institute. All calculations were carried out at the Center for Computational Innovations at Rensselaer Polytechnic Institute.

[1] J. Hong, C. Jin, J. Yuan, and Z. Zhang, Adv. Mater. **29**, 1606434 (2017).
[2] D. Wang, X.-B. Li, D. Han, W. Q. Tian, and H.-B. Sun, Nano Today **16**, 30 (2017).
[3] H. I. Rasool, C. Ophus, and A. Zettl, Adv. Mater. **27**, 5771 (2015).
[4] Z. Shi and C. V. Singh, Nanoscale **9**, 7055 (2017).
[5] W. Zhou, X. Zou, S. Najmaei, Z. Liu, Y. Shi, J. Kong, J. Lou, P. M. Ajayan, B. I. Yakobson, and J.-C. Idrobo, Nano Lett. **13**, 2615 (2013).
[6] H. Qiu, T. Xu, Z. Wang, W. Ren, H. Nan, Z. Ni, Q. Chen, S. Yuan, F. Miao, F. Song *et al.*, Nat. Commun. **4**, 2642 (2013).
[7] S. Refaely-Abramson, D. Y. Qiu, S. G. Louie, and J. B. Neaton, Phys. Rev. Lett. **121**, 167402 (2018).
[8] D. Wang, D. Han, D. West, N.-K. Chen, S.-Y. Xie, W. Q. Tian, V. Meunier, S. Zhang, and X.-B. Li, npj Comput. Mater. **5**, 8 (2019).
[9] H. Ardekani, R. Younts, Y. Yu, L. Cao, and K. Gundogdu, ACS Appl. Mater. Interfaces **11**, 38240 (2019).
[10] C. Si, D. Choe, W. Xie, H. Wang, Z. Sun, J. Bang, and S. Zhang, Nano Lett. **19**, 3612 (2019).
[11] D. Wang, X.-B. Li, and H.-B. Sun, Nanoscale **9**, 11619 (2017).
[12] S. Zhou, S. Wang, Z. Shi, H. Sawada, A. I. Kirkland, J. Li, and J. H. Warner, Nanoscale **10**, 16692 (2018).
[13] R. Frisenda, A. J. Molina-Mendoza, T. Mueller, A. Castellanos-Gomez, and H. S. van der Zant, Chem. Soc. Rev. **47**, 3339 (2018).
[14] K. Zhang, B. M. Bersch, J. Joshi, R. Addou, C. R. Cormier, C. Zhang, K. Xu, N. C. Briggs, K. Wang, S. Subramanian *et al.*, Adv. Funct. Mater. **28**, 1706950 (2018).
[15] J. S. Park, S. Kim, Z. Xie, and A. Walsh, Nat. Rev. Mater. **3**, 194 (2018).
[16] G. Grosso, H. Moon, B. Lienhard, S. Ali, D. K. Efetov, M. M. Furchi, P. Jarillo-Herrero, M. J. Ford, I. Aharonovich, and D. Englund, Nat. Commun. **8**, 705 (2017).
[17] T. T. Tran, C. Elbadawi, D. Totonjian, C. J. Lobo, G. Grosso, H. Moon, D. R. Englund, M. J. Ford, I. Aharonovich, and M. Toth, ACS Nano **10**, 7331 (2016).

[18] J. Klein, M. Lorke, M. Florian, F. Sigger, L. Sigl, S. Rey, J. Wierzbowski, J. Cerne, K. Müller, E. Mitterreiter *et al.*, Nat. Commu. **10**, 2755 (2019).
[19] T. T. Tran, K. Bray, M. J. Ford, M. Toth, and I. Aharonovich, Nat. Nanotechnol. **11**, 37 (2016).
[20] D. Wang, D. Han, X.-B. Li, S.-Y. Xie, N.-K. Chen, W. Q. Tian, D. West, H.-B. Sun, and S. B. Zhang, Phys. Rev. Lett. **114**, 196801 (2015).
[21] R. Sundararaman and Y. Ping, J. Chem. Phys. **146**, 104109 (2017).
[22] F. Wu, A. Galatas, R. Sundararaman, D. Rocca, and Y. Ping, Phys. Rev. Mater. **1**, 071001 (2017).
[23] D. Wang, D. Han, X.-B. Li, N.-K. Chen, D. West, V. Meunier, S. Zhang, and H.-B. Sun, Phys. Rev. B **96**, 155424 (2017).
[24] H.-P. Komsa and A. Pasquarello, Phys. Rev. Lett. **110**, 095505 (2013).
[25] H.-P. Komsa, N. Berseneva, A. V. Krasheninnikov, and R. M. Nieminen, Phys. Rev. X **4**, 031044 (2014).
[26] M. H. Naik and M. Jain, Comput. Phys. Commun. **226**, 114 (2018).
[27] C. Freysoldt and J. Neugebauer, Phys. Rev. B **97**, 205425 (2018).
[28] M. H. Naik and M. Jain, Phys. Rev. Mater. **2**, 084002 (2018).
[29] J.-Y. Noh, H. Kim, M. Park, and Y.-S. Kim, Phys. Rev. B **92**, 115431 (2015).
[30] J. Ma, Z. G. Yu, and Y.-W. Zhang, Phys. Rev. B **95**, 165447 (2017).
[31] A. Singh, A. Manjanath, and A. K. Singh, J. Phys. Chem. C **122**, 24475 (2018).
[32] M. S. Hybertsen and S. G. Louie, Phys. Rev. B **34**, 5390 (1986).
[33] D. Wang and R. Sundararaman, Phys. Rev. Mater. **3**, 083803 (2019).
[34] S. B. Zhang and J. E. Northrup, Phys. Rev. Lett. **67**, 2339 (1991).
[35] S.-H. Wei, Comput. Mater. Sci. **30**, 337 (2004).
[36] C. G. Van de Walle and J. Neugebauer, J. Appl. Phys. **95**, 3851 (2004).
[37] See Supplemental Material at http://link.aps.org/supplemental/10.1103/PhysRevB.101.054103 for additional computational details and complete tables of defect ionization energies and band positions.
[38] R. Sundararaman, K. A. Schwarz, K. Letchworth-Weaver, and T. A. Arias, J. Chem. Phys. **142**, 054102 (2015).
[39] R. Sundararaman and W. A. Goddard, J. Chem. Phys. **142**, 064107 (2015).
[40] D. Gunceler, K. Letchworth-Weaver, R. Sundararaman, K. A. Schwarz, and T. A. Arias, Model. Simul. Mater. Sci. Eng. **21**, 074005 (2013).
[41] J. Tomasi, B. Mennucci, and R. Cammi, Chem. Rev. **105**, 2999 (2005).
[42] A. V. Marenich, C. J. Cramer, and D. G. Truhlar, J. Phys. Chem. B **113**, 6378 (2009).
[43] O. Andreussi, I. Dabo, and N. Marzari, J. Chem. Phys **136**, 064102 (2012).
[44] R. Sundararaman, K. Letchworth-Weaver, K. A. Schwarz, D. Gunceler, Y. Ozhabes, and T. Arias, SoftwareX **6**, 278 (2017).
[45] K. F. Garrity, J. W. Bennett, K. M. Rabe, and D. Vanderbilt, Comput. Mater. Sci. **81**, 446 (2014).
[46] J. P. Perdew, K. Burke, and M. Ernzerhof, Phys. Rev. Lett. **77**, 3865 (1996).
[47] R. Sundararaman and T. A. Arias, Phys. Rev. B **87**, 165122 (2013).
[48] G. Constantinescu, A. Kuc, and T. Heine, Phys. Rev. Lett. **111**, 036104 (2013).
[49] S. Grimme, J. Comput. Chem **27**, 1787 (2006).
[50] J. Deslippe, G. Samsonidze, D. A. Strubbe, M. Jain, M. L. Cohen, and S. G. Louie, Comput. Phys. Commun. **183**, 1269 (2012).
[51] M. Schlipf and F. Gygi, Comput. Phys. Commun. **196**, 36 (2015).
[52] C. Freysoldt, P. Eggert, P. Rinke, A. Schindlmayr, R. Godby, and M. Scheffler, Comput. Phys. Commun. **176**, 1 (2007).
[53] C. Freysoldt, P. Eggert, P. Rinke, A. Schindlmayr, and M. Scheffler, Phys. Rev. B **77**, 235428 (2008).
[54] D. Y. Qiu, F. H. da Jornada, and S. G. Louie, Phys. Rev. B **93**, 235435 (2016).
[55] Y.-N. Xu and W. Y. Ching, Phys. Rev. B **44**, 7787 (1991).
[56] D. West, Y. Sun, and S. Zhang, Appl. Phys. Lett. **101**, 082105 (2012).
[57] Z. Shi, E. Tsymbalov, M. Dao, S. Suresh, A. Shapeev, and J. Li, Proc. Natl. Acad. Sci. USA **116**, 4117 (2019).
[58] T. J. Smart, F. Wu, M. Govoni, and Y. Ping, Phys. Rev. Mater. **2**, 124002 (2018).